Data-based diffraction kernels for surface waves from convolution and correlation processes through active seismic interferometry

Malgorzata Chmiel,[1,2] Philippe Roux,[2] Philippe Herrmann,[1] Baptiste Rondeleux[1] and Marc Wathelet[2]

[1]*CGG, 27 Avenue Carnot, 91300 Massy, France. E-mail: mchmiel@sisprobe.com*
[2]*ISTerre, Université Grenoble Alpes, CNRS UMR 5275, 1381 Rue de la piscine, 38610 Gières, France*

SUMMARY

We investigated the construction of diffraction kernels (DKs) for surface waves using two-point convolution and/or correlation from land active seismic data recorded in the context of exploration geophysics. The high density of controlled sources and receivers, combined with the application of the reciprocity principle, allows us to retrieve 2-D phase-oscillation DKs of surface waves between any two source or receiver points in the medium at each frequency (up to 15 Hz, at least). These DKs are purely data based as no model calculations and no synthetic data are needed. They naturally emerge from the interference patterns of the recorded wavefields projected on the dense array of sources and/or receivers. The DKs are used to obtain multimode dispersion relations of Rayleigh waves, from which near-surface shear velocity can be extracted. Using convolution versus correlation with a grid of active sources is an important step in understanding the physics of the retrieval of surface wave Green's functions. This provides the foundation for future studies based on noise sources or active sources with a sparse spatial distribution.

Key words: Interferometry; Seismic tomography; Surface waves and free oscillations; Wave propagation.

1 INTRODUCTION

The construction of a subsurface velocity model is an important issue in different domains (e.g. seismology, civil engineering, seismic exploration). In particular, the near surface is classically characterized by high structural complexity that is due to multilayered sediments. Surface waves sample the shallow structures and can provide useful information on local subsurface heterogeneities. However, obtaining phase-velocity and group-velocity maps for surface waves can be challenging, due to the presence of fundamental and higher-order surface wave modes that are difficult to identify.

New possibilities for imaging of the Earth structure have emerged with surface wave tomography from ambient seismic noise (e.g. Shapiro & Campillo 2004; Sabra *et al.* 2005; Shapiro *et al.* 2005; Brenguier *et al.* 2007). Surface waves are most easily extracted using noise interferometry, because they dominate the wavefields recorded on receivers located at the surface (Shapiro *et al.* 2005).

Traditionally, ray theory is used to build a forward model in the seismic tomography process for surface waves, which leads to images of the subsurface (e.g. Barmin *et al.* 2001). This can provide good results if the scale of the heterogeneities in the medium is larger than the wavelength. If the scale of the heterogeneities is similar to the wavelength or smaller, the sensitivity kernels account for the

finite frequency interference effects, as they recognize the frequency dependence of both traveltime and amplitude (e.g. Marquering *et al.* 1999; Dahlen *et al.* 2000; Zhao *et al.* 2000).

Sensitivity kernels can reflect the sensitivity of a wavefield to local variations in different parameters, such as density, velocity, porosity and anisotropy. In practice, surface wave sensitivity kernels have been derived from perturbation theory in the framework of the single-scattering Born approximation (Zhou *et al.* 2004; Yang & Forsyth 2006). In 2005, Tromp *et al.* showed the connection between seismic waveform tomography, adjoint models and sensitivity kernels through the interactions between the 'forward' and 'adjoint' wavefields (Tarantola 1988; Tromp *et al.* 2005; Fichtner *et al.* 2006; Liu & Tromp 2006). The principal application of adjoint models is sensitivity analysis. An adjoint model provides a first-order approximation for the local parameter sensitivity in a nonlinear model (Errico 1997). The adjoint wavefield is excited by an adjoint source and travels backward in time (de Vos *et al.* 2013). For surface waves, this requires an adequate 2-D synthetic subsurface model, and it can often be computationally challenging. The sensitivity kernels arise from the interference pattern between the forward wavefield and the adjoint wavefield.

As an alternative to complex synthetic model computations, the development of dense seismic arrays opened a road to innovative surface wave tomography methods (e.g. eikonal tomography: Lin

et al. 2009). Following this approach, sensitivity kernels were proposed through exploitation of ambient-noise cross-correlations on a dense seismic array (e.g. Tromp *et al.* 2010) and of teleseismic earthquakes (e.g. Lin & Ritzwoller 2010). In the latter case, the accuracy of the empirical sensitivity kernels depends on both the spatial sampling proposed by the array of sensors and the robustness of the phase or traveltime maps. Indeed, traveltime (or phase delay) measurements can be relatively challenging when dealing with complex waveforms and cycle-skipping issues.

In this study, we build data-based diffraction kernels (DKs) for surface waves that result either from correlation or convolution process. The DKs are computed at one frequency between two receivers and one source that spatially scan a large 2-D surface. In the case of convolution, the DK exactly matches the sensitivity kernel definition for surface waves. In the case of correlation, the DK reveals phase oscillations in connection with the stationary-phase theorem that is classically invoked to extract surface wave traveltime arrivals from noise interferometry (Campillo & Roux 2014). In practice, we use a data set from 51 808 active sources (seismic vibrator trucks) that was recorded by 10 710 vertical receivers. The sources were spaced at intervals of 30 m (in both dimensions), and the receivers were placed in parallel lines (150 m/30 m in the *x*/*y* directions, respectively). Seismic acquisition with active, controlled and spatially dense source arrays offers rare but innovative possibilities when it comes to seismic interferometry and tomography. In particular, we benefit from this densely sampled active-source array to explore both convolution-based and correlation-based interferometry. The large number of sources and receivers, combined with the application of the reciprocity principle, allow us to retrieve 2-D DKs, of surface waves between any two source or receiver points in the medium at each frequency (up to 15 Hz, at least). These DKs are purely data based, as no model calculations and no synthetic data are needed. As described in the literature (e.g. Walker 2012; Fichtner *et al.* 2017), these emerge from the interference pattern between the recorded wavefields dominated by surface waves.

In the following, we theoretically investigate the role of the mathematical operations (i.e. correlation and convolution) in seismic interferometry with active sources. Next, we use correlation and convolution to extract data-based DKs for Rayleigh waves. These data-based DKs are finally used for surface wave phase-velocity tomography, based on the DK modelling. This study provides the foundation of future studies based on noise sources or active sources with a sparse spatial distribution.

2 METHODS

The data used in this study were acquired during a field test over a 42-km^2 area in the context of geophysics exploration (Fig. 1a). The data were from 51 808 active sources (seismic vibrator trucks) that were recorded by 10 710 vertical geophones. A seismic vibrator is a truck that generates a long and low-power broad-band frequency sweep, from 2 to 100 Hz (Postel *et al.* 2005). The received signals are then cross-correlated with the emitted sweep to construct the subsurface impulse response, from which surface waves and reflection events are revealed (Fig. 2). The source spacing is the same in both the *x* and *y* directions (30 m), which is known as 'carpet shooting'. The receivers are positioned in parallel lines with a spacing of 150 m in the *x* direction and 30 m in the *y* direction (Fig. 1b). One recorded trace is the sum of six tightly clustered vertical geophones.

Seismic interferometry can be used with either active sources or passive sources (Schuster *et al.* 2008). Bakulin and Calvert (2004) showed possible applications of interferometry using active sources in the context of geophysics exploration. With noise interferometry, long averaging times are needed for the correlation function to converge towards the surface wave Green's function under the condition of azimuthal averaging of the noise source distribution. In the case of an active seismic experiment, the long recording time is traded for the regular spatial distribution of the sources and/or receivers. In practice, the data are recorded separately for each shot at each source position, and the length of one recording is a few seconds (here, 5 s). The azimuthal averaging criterion is fulfilled due to the dense distribution of sources and receivers, the locations of which are known precisely. Seismic acquisition with active sources has more possibilities when it comes to interferometry, as the use of sources with absolute time control makes it possible to recover the surface wave Green's functions between two points using either correlation or convolution.

In classical seismic acquisition at the Earth surface, the surface waves generated by the vibrator truck are often more energetic than the reflection and refraction events, and they are the dominant arrivals in the recorded data (Fig. 2). In this paper, we limit our study to surface wave interferometry from the wavefield analysis that was performed on interleaved source and receiver arrays.

The reciprocity principle states that the traveltime along a given ray path is the same regardless of the direction of travel (Sheriff & Geldart 1995). In other words, if any source and any receiver are interchanged (under some polarization conditions: for example, a vertical force on the source side and a vertical receiver), the same waveforms will be observed. This principle can be used to enlarge the data collection. The representation theorem that is classically invoked for Green's function retrieval from sets of cross-correlation functions is built on the reciprocity principle (Wapenaar 2004). In practice, this means that the active seismic data can be represented in two different formats: the source gather (Fig. 3a) and the receiver gather (Fig. 3b). The source gather shows the wavefield generated by one point source and recorded simultaneously on a set of receivers. Contrarily, the receiver gather represents the wavefield generated by each point source and recorded at one reference receiver. In other words, the reference receiver acts as a virtual point source and the carpet/grid of sources at the surface plays the role of virtual receivers that were activated one at a time.

In this study, the spatial sampling of the wavefield is optimal in the source domain, as it allows the phase changes of the recorded wavefield to be tracked with 30-m spatial accuracy in both the *x* and *y* directions (Figs 1 and 3b). Note that the source gather in Fig. 3(a) shows coherent noise due to its temporal continuity and the presence of other sources at the same time (i.e. simultaneous shooting). The receiver gather retains the spatial continuity, although it lacks the temporal continuity, which results in a smoother spatial representation only polluted by random, low-amplitude, incoherent noise (Fig. 3b).

2.1 Interferometry by convolution and correlation

Acoustic or elastic wave interferometry provides a measure of the wavefield between two receivers by applying cross-correlation, deconvolution (e.g. Wapenaar *et al.* 2008) or even convolution (e.g. Roux & Fink 2003; Slob *et al.* 2007), to the wavefield recordings at these two points (Duguid *et al.* 2011). When applied to seismic recordings, surface wave interferometry takes advantage of the

(a) • 51 808 sources • 10 710 vertical geophones   (b)
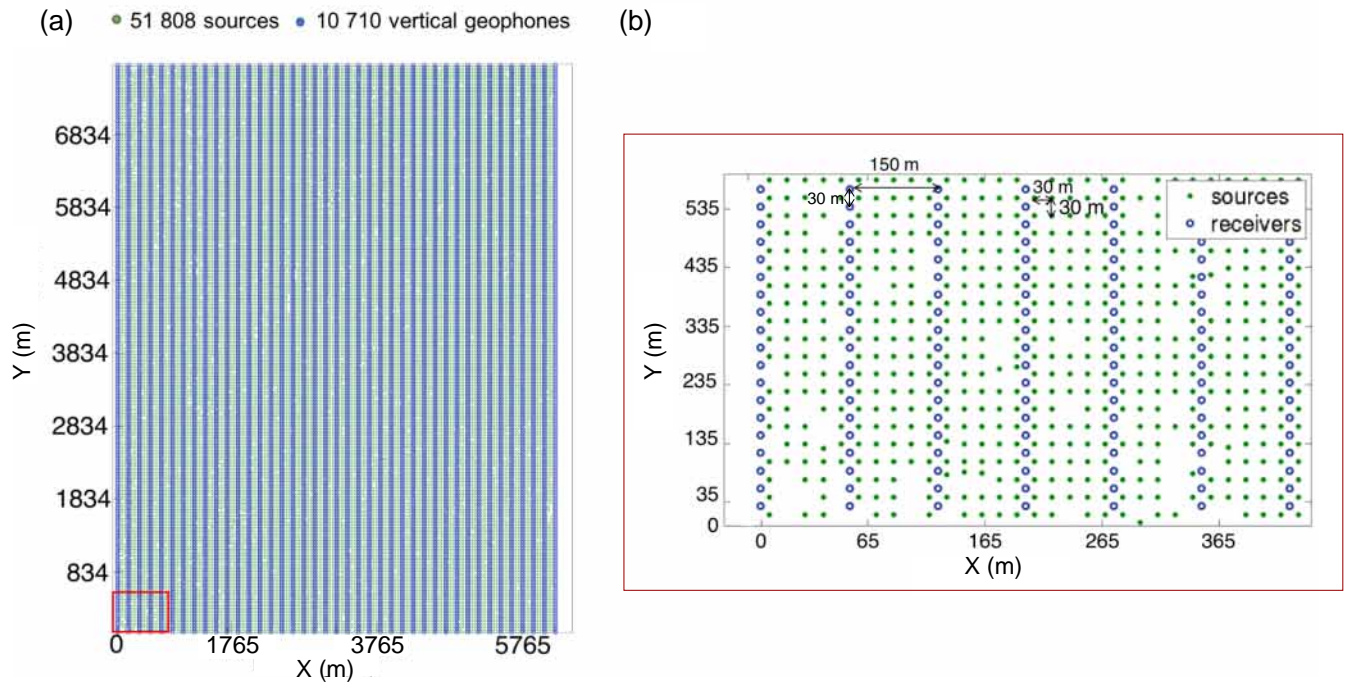
Figure 1. Active seismic acquisition. In this survey, a grid of active sources was applied during an experimental field test in the context of geophysics exploration. The *x–y* coordinates are relative to the position of the first source. (a) The full array of the active seismic survey. (b) Zoom of the bottom-left area of 2 km^2 [red box in (a)]. The source spacing is the same in the *x* and *y* directions (30 m). The receivers were placed in parallel lines with a spacing of 150 m in the *x* direction and 30 m in the *y* direction.
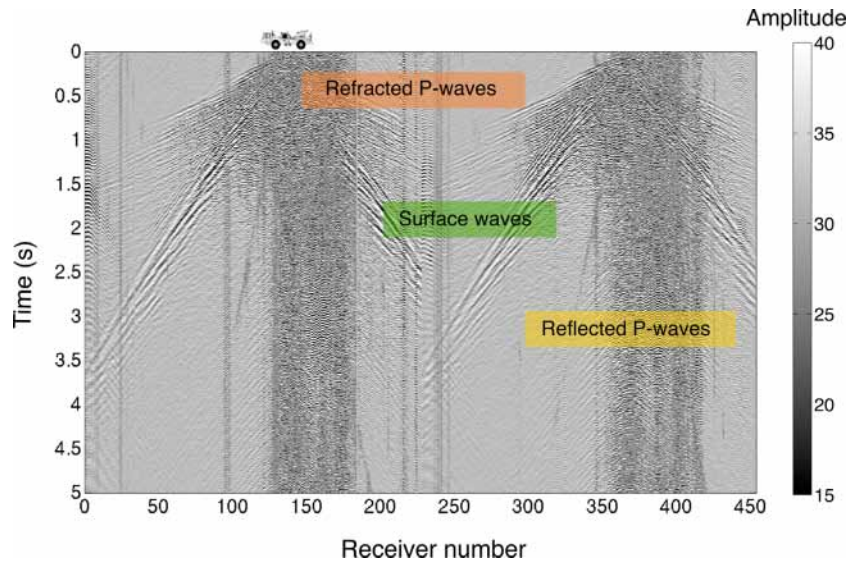

Figure 2. Active seismic data. Raw data for the source and two lines of receivers. Note that the surface waves are more energetic than the body waves.

correlation process to recover traveltime information from incoherent noise sources (Sabra *et al.* 2005; Campillo & Roux 2014). Indeed, because of the phase cancellation in the correlation process, the origin time of the noise sources is not required, and the seismic noise can be used for surface wave tomography. On the contrary, surface wave interferometry based on convolution requires sources that are synchronized with receivers, with accurate absolute time control. In this project, we benefit from the large set of perfectly synchronized active sources and receivers to explore both the convolution and the correlation approaches in surface wave interferometry.

We now revisit the theoretical approach that leads to the surface wave Green's function retrieval from controlled sources in a 2-D medium with both convolution and correlation schemes. The surface wave Green's function can be obtained from the scalar Green's function in 2-D (defined as G^{2D}, see Tromp & Dahlen 1993; Section 5; Boschi & Weemstra 2015). The analysis of 2-D wavefields hold, therefore, for Rayleigh waves propagating in a 3-D medium (in the Earth) and measure on the vertical component of seismograms, as far as the phase is concerned. The Rayleigh wave approach of Snieder (2004) is also based on this idea. Halliday & Curtis (2008) explore the effects of subsurface sources on Green's
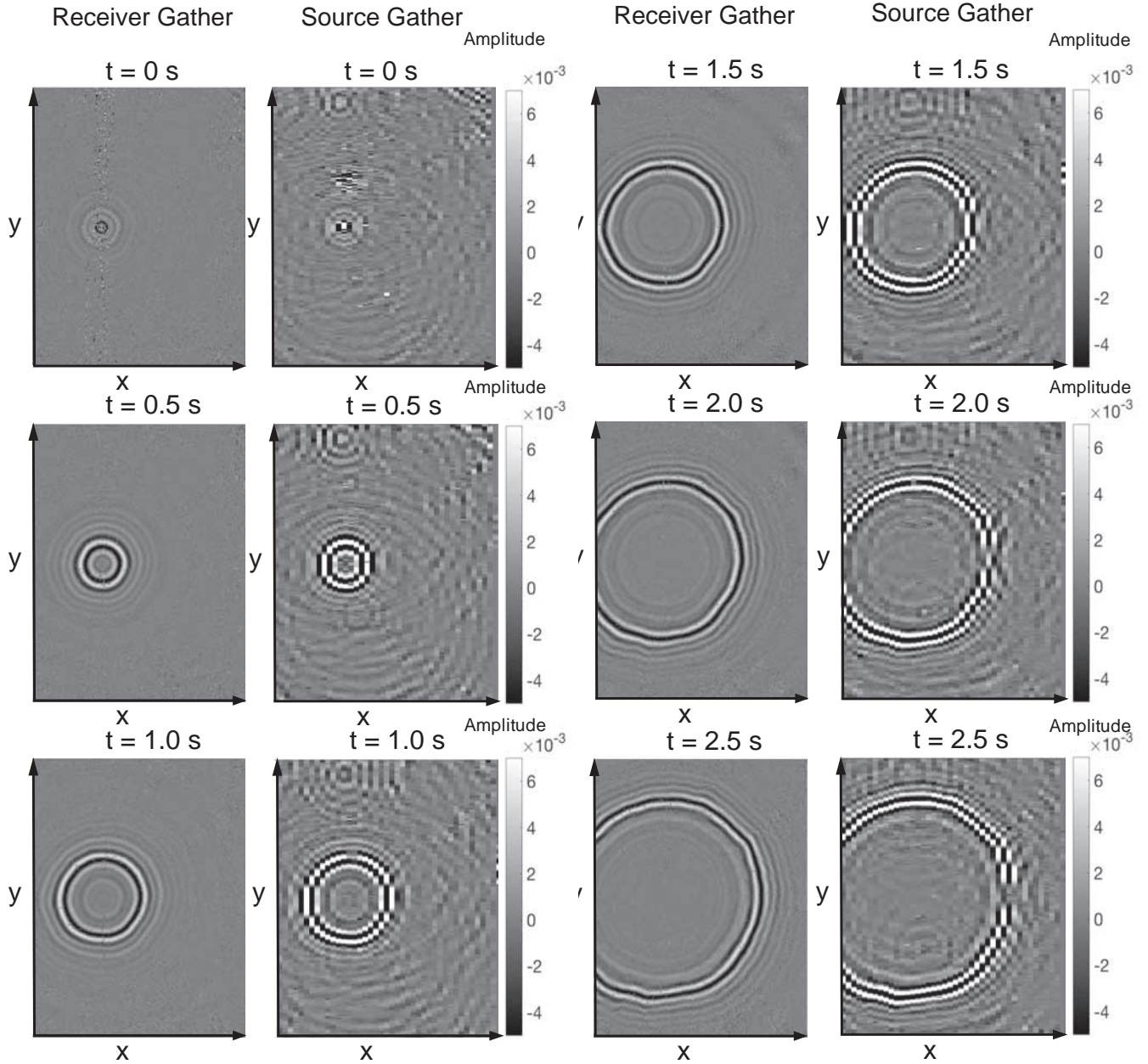
Figure 3. Source (a) and receiver (b) gather collections with time slices taken at 0, 0.5, 1, 1.5, 2 and 2.5 s in the 2–6 Hz frequency band. Using the reciprocity principle, each slice represents the wavefield excited by each source and recorded at one reference receiver.

function reconstruction; their results are consistent with those of Snieder (2004) whenever their setup is a uniform source distribution over the Earth's surface.

In practice, we consider a free space with attenuation and geometry with two receivers *1* (in $\mathbf{r}_1$) and *2* (in $\mathbf{r}_2$) and a large set of sources *s* (in $\mathbf{r}_s$) that covers the whole 2-D surface. Note that as shown in Fig. 3, the roles of the sources and receivers can be physically interchanged according to the reciprocity principle. We now deal with the average correlation and/or convolution of the signals recorded at *1* and *2* from each single source *s*. Through the spatial integration over all of the sources, different studies have demonstrated that the time derivative of the correlation function provides an estimate of the causal and anticausal Green's functions (Snieder 2004; Roux *et al.* 2005; Campillo & Roux 2014; Boschi & Weemstra 2015), as

given in eq. (1):

$$\frac{\mathrm{d}}{\mathrm{d}t}\mathrm{Corr}_{1,2}(t) \sim \left(G_{1,2}^{2\mathrm{D}}(t) - G_{2,1}^{2\mathrm{D}}(-t)\right). \tag{1}$$

Similarly, an equivalent result is obtained for the convolution function, as given in eq. (2):

$$\frac{\mathrm{d}}{\mathrm{d}t}\mathrm{Conv}_{1,2}(t) \sim G_{1,2}^{2\mathrm{D}}(t). \tag{2}$$

Despite a clear analogy between these two results, there are major differences between the correlation and convolution processes. While the correlation deals with the subtraction of traveltimes between each source *s* and receivers in *1* and *2*, the convolution performs the addition of these traveltimes. This implies that the convolution process requires perfect synchronization between the

controlled sources and receivers when the correlation process can be performed with incoherent noise sources.

As correlation can be interpreted through time reversal, the focal-point mechanism between points *1* and *2* results from the summation of a convergent and divergent Green's function generated by the time-reversal mirror built from the set of sources *s* outside these two points. On the contrary, the convolution process mimics Huygens's theorem between receiver points *1* and *2* through a constructive interference process, which is generated this time at each source *s* in between these two points.

3 DATA-BASED DKS

It can be seen from eqs (1) and (2) that both the correlation and convolution processes between two receivers in *1* and *2* are strongly connected to the Green's function retrieval when averaged over a dense map of point sources. The Green's function perturbation associated to a local change that classically leads to the sensitivity kernel formulation shows a direct connection with the convolution process (Spetzler *et al.* 2002; Zhou *et al.* 2004; Yoshizawa & Kennett 2005; Peter *et al.* 2007, Marandet *et al.* 2011). We propose here to generalize the concept of DKs to the correlation process, and to illustrate both of the DKs that are obtained from either convolution or correlation through experimental measurements.

In practice, we define two types of DKs, both of which are limited to phase perturbations, one for convolution (eq. 3) and one for correlation (eq. 4):

$$K_{\mathrm{conv}}\left(\omega; \mathbf{r}_1, \mathbf{r}_s, \mathbf{r}_2\right) = G\left(\omega; \mathbf{r}_s, \mathbf{r}_1\right) G\left(\omega; \mathbf{r}_s, \mathbf{r}_2\right), \tag{3}$$

$$K_{\mathrm{corr}}\left(\omega; \mathbf{r}_1, \mathbf{r}_s, \mathbf{r}_2\right) = G\left(\omega; \mathbf{r}_s, \mathbf{r}_1\right) G^*\left(\omega; \mathbf{r}_s, \mathbf{r}_2\right), \tag{4}$$

where $\mathbf{r}_1$ and $\mathbf{r}_2$ correspond to receiver points in *1* and *2*, and $\mathbf{r}_s$ to sources *s*.

Eqs (3) and (4) mean that we use the interference pattern between two empirical wavefields to retrieve data-based DKs. These physically correspond to a spatial representation of the correlation and convolution processes described above, prior to the spatial averaging performed on the set of sources *s* (eqs 1 and 2). As we choose to limit this study to phase variations, spectral whitening is applied to the received data at each frequency, which is equivalent to saying that the narrow-band time-domain correlation and convolution functions are normalized, for a source in *s*, by the energy of the received signals in *1* and *2*. Normalized cross-correlations are also defined in the literature as coherence function (Jones 2000). Playing with phase-only DKs is a way to cancel out amplitude-related issues associated to the physical coupling of both geophones and active sources to the ground. This emphasizes the dominant role played by local velocity variations on the traveltimes, which is the main goal in surface wave tomography inversion. On the other hand, this prevents investigation into local attenuation or damping, which can be considered as a second-order effect at low frequencies (<10 Hz).

Fig. 4 shows the data-based DKs for both correlation and convolution calculated at a single frequency of 3.8 Hz. These data-based DKs are complex numbers; here, we represent the imaginary part for correlation and the real part for convolution.

As shown in eqs (3) and (4), the DKs calculated with correlation are based on phase differences, and the DKs calculated with convolution are based on phase addition. This explains why the convolution DK in Fig. 4(a) shows faster phase oscillations than the correlation DKs in Figs 4(b) and (c). The convolution DK reveals the primary influence area in between the two receivers (defined

here as the inner DK, or the first Fresnel zone; e.g. Yoshizawa & Kennett 2002). Instead, the correlation DKs demonstrate the presence of stationary-phase areas (defined here as the outer DK) in the alignment of the two receivers (Roux & Kuperman 2004; Snieder 2004; Roux *et al.* 2005; Walker 2012). Note that the shape of the inner DK is elliptical, and the shape of the outer DKs is hyperbolic.

In Fig. 5, the DKs were integrated over a given frequency band $(\omega_1-\omega_2)$ for convolution and correlation around the stationary time τ_{12}. The coherent summation of the frequency-dependent DKs over the frequency band results in smoothing of the frequency-dependent phase oscillations outside the first Fresnel zone (for convolution) and the end-fire lobe (for correlation), which is in agreement with the stationary-phase theorem (Roux & Kuperman 2004; Snieder 2004). In a recent paper, Fichtner *et al.* (2017) provide in Fig. 10 an analogue spatial representation of 'source kernels' for the noise correlation process computed for a band-limited spectrum at different times τ.

Note that Fig. 5(a) is extracted at slightly different traveltimes to Figs 5(b) and (c). Outside of experimental uncertainties, this traveltime difference might be due to a slight phase shift between convolution and correlation in Green's function reconstruction that is associated to the medium attenuation in 3-D acoustic configurations.

The geometry of DKs depends on several factors, including the frequency and the distance between the receivers. Figs 6 and 7 show the spatial evolution of the inner and outer DKs for convolution and correlation, at a frequency 4.2 Hz. The position of receiver *1* remains unchanged when receiver *2* is moved away, while keeping the same *1–2* azimuth (distance 870, 1443, 2100 and 2737 m). In the case of the convolution DK, there is broadening of the first Fresnel zone with an increase in the offset between the two receivers, and as a consequence, a decrease in the number of phase oscillations.

In contrast, in Fig. 7 there is a narrowing of the stationary-phase zone (also called the end-fire lobe) with an increase in the offset between the two receivers with the correlation DK. There is also an increase in the phase oscillations in between the sensors.

Finally, Fig. 8 shows the frequency evolution of the data-based DKs for convolution and correlation at two different frequencies. In both cases, the number of phase oscillations increases with frequency, and the sizes of the first Fresnel zone (for convolution) or stationary-phase zone (for correlation) become narrower as the surface wave wavelength decreases. At 2.7 Hz, the correlation DK (Fig. 8c) shows some deformation of the interference fringes that is due to local phase-velocity anomalies. We note that these phase fluctuations are more difficult to observe in the convolution DK (Fig. 8a). This means that the spatial resolution of the correlation and convolution DKs are different at the same frequency. Note that for correlation here, the calculation of the real, symmetric part of the DK is shown.

As empirical DKs carry the footprint of the velocity fluctuations in the medium, we propose in the following an inversion algorithm to extract dispersion relations for phase velocities from the combination of convolution and correlation DKs.

4 PHASE-VELOCITY INVERSION WITH HYPERBOLIC AND ELLIPTICAL TRANSFORMATIONS

The inversion process is performed for each pair of receivers from the data-based DKs. The idea is to project data-based DKs into the modelled frequency-phase-velocity space. To do so, we model
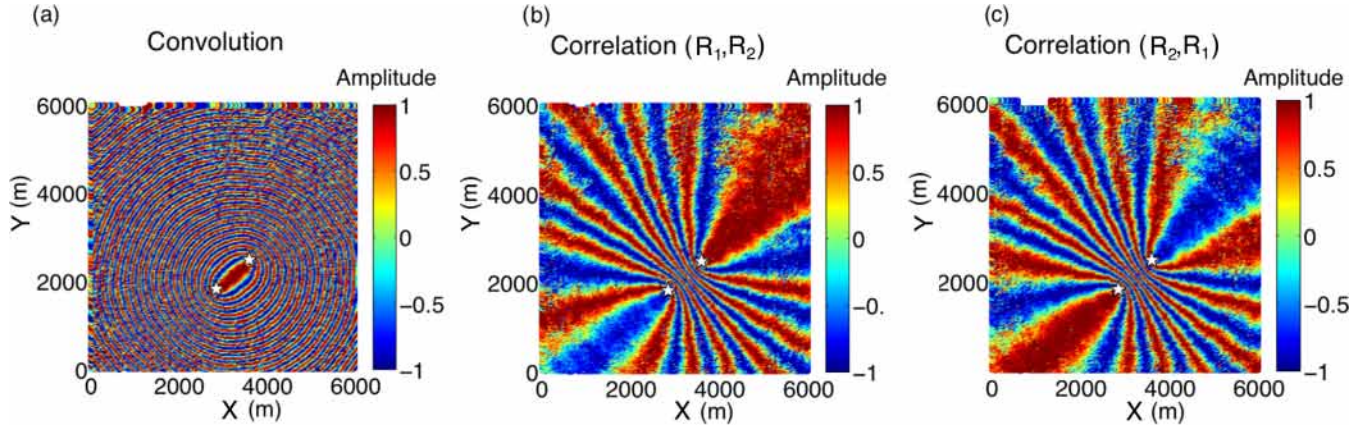
Figure 4. Data-based DKs at a frequency of 3.8 Hz for convolution (a) and correlation (b and c). The distance between the two receivers was 990 m. The x and y coordinates correspond to source positions $\mathbf{r}_s$. The DKs are defined as a spatial representation of phase coherence at a given frequency (only the real part of the convolution-based kernel function and the imaginary part of the correlation-based kernel are represented; see eqs (1) and (2). In (a), the zone over which the surface waves are coherent in phase is defined as the first Fresnel zone, where the convolved wavefields interfere in a coherent way. In (b) and (c), all of the sources located within the first phase oscillation belong to the stationary-phase zone.
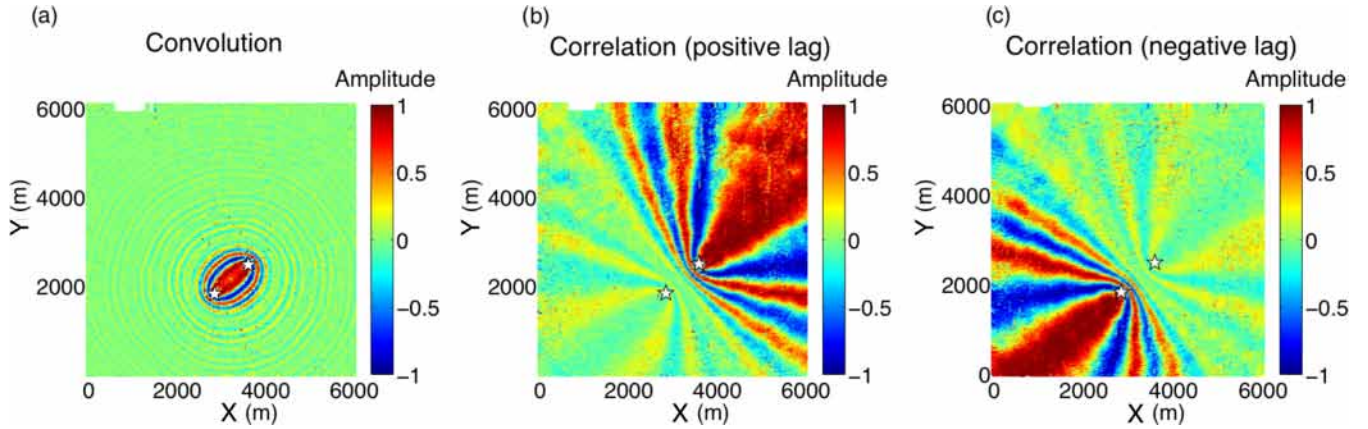
Figure 5. Time-domain data-based DKs in the frequency band (3–4) Hz for convolution (a) and correlation (b and c) calculated at the traveltime τ_{12} between the receivers. The distance between the two receivers was 990 m. The x and y coordinates correspond to source positions $\mathbf{r}_s$. Data-based DKs are defined only at positive times for convolution, and at both negative and positive times for correlation. The traveltime τ_{12} corresponds to the maximum of the stacked convolution or correlation functions (eqs 1 and 2). In practice, $\tau_{12} = 0.85$ s for the convolution kernel and $\tau_{12} = \pm 0.84$ s (causal and anticausal parts) for the correlation kernel.

theoretical DKs parametrized by the surface wave velocity on which the empirical DKs are projected. The projection or inversion process is applied to the set of sources s for which the empirical DKs are measured. At each frequency w, we define a matrix representation between the phase-only observed DK $\mathbf{K}(\omega, \mathbf{r}_s)$ and the unknown dispersion relation $\mathbf{D}(\omega; c)$, as given in eq. (5):

$$\mathbf{K}(\omega; \mathbf{r}_s) = \mathrm{A}(\omega; \mathbf{r}_s; c) \cdot \mathbf{D}(\omega; c). \tag{5}$$

The 2-D transformation matrix $\mathrm{A}(\omega; \mathbf{r}_s; c)$ has one dimension connected to the spatial domain of the sources $\mathbf{r}_s$ and the other with the phase-velocity domain c. We introduce two different transformation matrices for correlation (i.e. hyperbolic transformation) and convolution (i.e. elliptical transformation).

The hyperbolic transformation is based on phase differences, as given in eq. (6):

$$\mathrm{A}_{\mathrm{corr}}(\omega; \mathbf{r}_s; c) = \exp\left(\frac{i\omega}{c}(|\mathbf{r}_s - \mathbf{r}_1| - |\mathbf{r}_s - \mathbf{r}_2|)\right), \tag{6}$$

whereas the elliptical transformation is based on phase additions, as given in eq. (7):

$$\mathrm{A}_{\mathrm{conv}}(\omega; \mathbf{r}_s; c) = \exp\left(\frac{i\omega}{c}(|\mathbf{r}_s - \mathbf{r}_1| + |\mathbf{r}_s - \mathbf{r}_2|)\right), \tag{7}$$

where $\mathbf{r}_1$, $\mathbf{r}_2$ are the positions of the receivers and $\mathbf{r}_s$ is the position of the source.

The least-squares estimation, which is also known as a minimizer of the residual sum of squared errors (Hastie *et al.* 2001), is $\|\mathrm{A}\mathbf{D} - \mathbf{K}^2\|$. The dispersion curve $\mathbf{D}$ is constructed by minimizing this expression with the use of correlation/convolution data-based DKs and the corresponding hyperbolic/elliptical transformation.

In practice, finding the least-squares estimate requires inversion of matrix $\mathrm{A}^{\mathrm{T}}\mathrm{A}$. However, this matrix can be singular, which causes difficulty for the inversion. One of the methods that addresses the numerical instability of matrix inversion is Tikhonov regularization (Boyd & Vandenberghe 2004), which consists of adding a small positive constant to the diagonal of $\mathrm{A}^{\mathrm{T}}\mathrm{A}$. This penalty term can be expressed with a L2-norm or a L1-norm. L2-norm regularization provides numerical stability, although it does not encourage sparsity
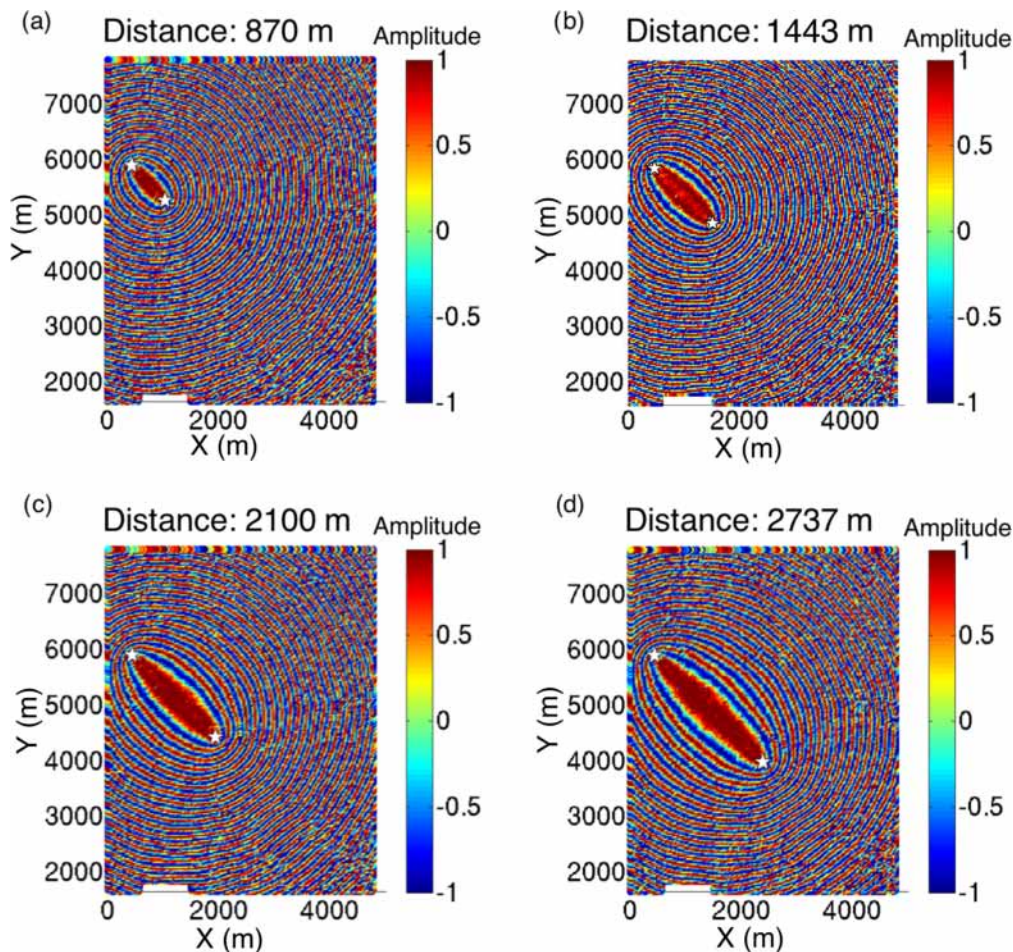
Figure 6. Data-based DKs for convolution at a frequency 4.2 Hz for two receivers separated by distances of 870 m (a), 1443 m (b), 2100 m (c) and 2737 m (d). The *x* and *y* coordinates correspond to source positions $\mathbf{r}_s$.

of the dispersion curve estimate **D** (Schmidt 2005; Guillouet *et al.* 2016), as shown in Fig. 9. Note that for both correlation and convolution processing, the dispersion relations were estimated from a limited number of Fresnel zones or stationary-phase areas (Figs 8b and d, dashed ellipse, hyperbola), as an optimal trade-off between resolution and robustness of the inversion process.

Dispersion of surface waves occurs in vertically stratified media, and can lead to the presence of higher-order modes. If the velocity of the upper layer is low enough to cause a complete reflection of both the *P* waves and the *SV* waves, then higher branches of Rayleigh waves are seen (Heaton 2005). These overtones provide important information on shallow structures and on the uniqueness of the inverted models (van Heijst & Woodhouse 1997). However, it might be difficult to invert higher modes, due to interference, simultaneous arrivals and overlap in the frequency domain.

The dispersion relations shown in Fig. 9 show a fundamental Rayleigh surface mode together with two higher-order overtones. The modes are relatively well separated, although there remains some interference between different mode branches. There are some discrepancies between the dispersion relations inverted from the correlation and convolution DKs. This might be due to the differences between the Fresnel zones and stationary-phase areas; that is, the inner and outer DKs. For correlation, the phase subtraction is a

more robust and stable operation at higher frequencies (>5 Hz) than the phase addition of the convolution process. On the other hand, convolution provides higher spatial resolution at lower frequencies (<5 Hz), as phase addition varies rapidly with distance, while the uncertainty linked to 2p phase jumps also increases with frequency in the same manner.

We now combine both the correlation and convolution DKs in the inversion process. Indeed, DKs extracted from convolution provide better resolution at lower frequencies, while DKs extracted from correlation provide robust results at higher frequencies. To use both the inner and outer DKs together, some weighting is introduced into the frequency domain. In practice, we give more weight to the convolution (ratio of 0.7) at frequencies up to 7.3 Hz, and more weight to the correlation (ratio of 0.95) at higher frequencies, with a smooth transition between the weights to minimize discontinuities.

Fig. 10(b) shows the joint dispersion curve analysis using L2-norm regularization. As mentioned before, the L1-norm regularization can enhance the sparsity of the solution. Nevertheless, the L1-norm regularization cannot be solved algebraically, which has led to the introduction of different techniques to determine the optimal parameters (Schmidt 2005). Estimation of least-squares parameters with the L1-norm was popularized under the names of
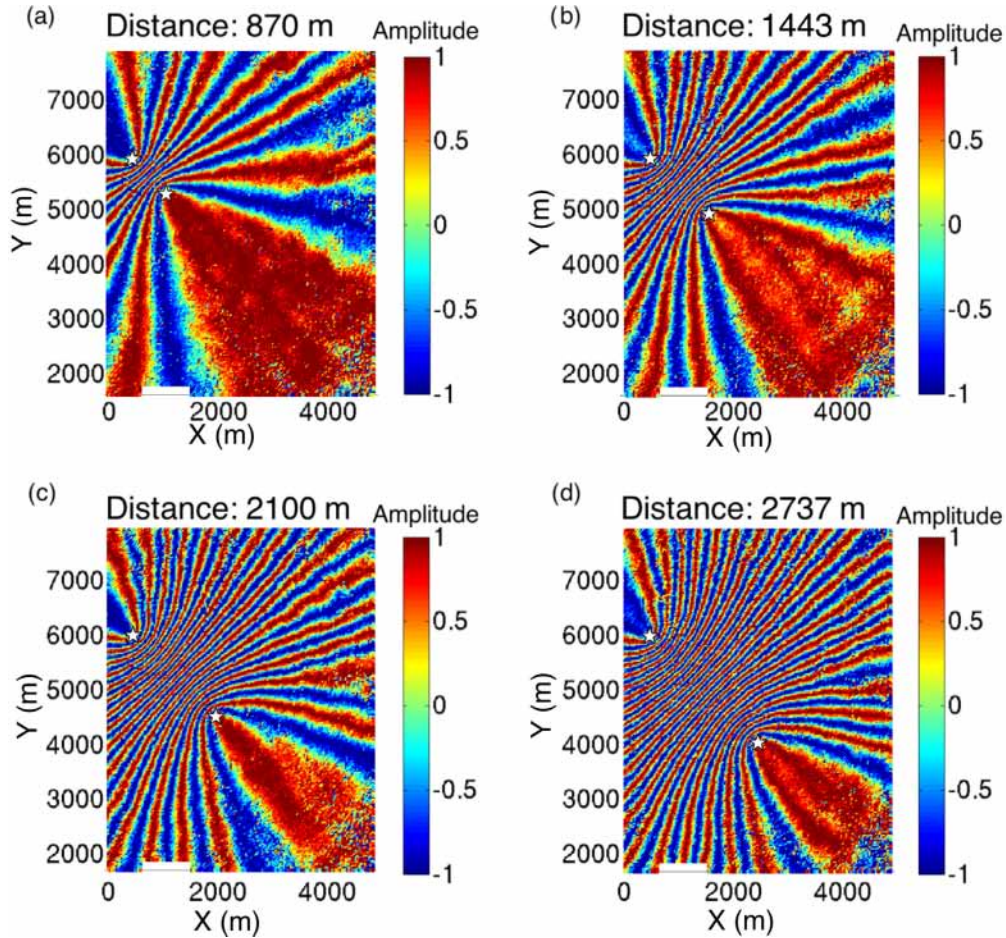
Figure 7. Data-based DKs for correlation (positive lag time) at a frequency 4.2 Hz for two receivers separated by distances of 870 m (a), 1443 m (b), 2100 m (c) and 2737 (d). The x and y coordinates correspond to source positions $\mathbf{r}_s$.

Least Absolute Selection and Shrinkage Operator (LASSO; Tibshirani 1996) and Basis Pursuit Denoising (Chen *et al.* 1999). Here, we empirically chose the shooting method for the LASSO minimization problem.

As expected, the joint inversion takes advantage of the correlation and convolution DKs to optimize the balance between resolution and robustness over a large frequency band (Fig. 10). Despite residual interference between different branches of the modes, the sparse solution (Fig. 10a) provides super-resolution, from which the frequency-dependent maxima of the multimodal dispersion relations can be easily picked.

In the following, the Dinver software (Wathelet *et al.* 2008) is used to invert the phase velocity dispersion of the surface waves obtained from the two receivers shown in Fig. 8. The objective is to determine the depth resolution and uncertainty for the *S*-wave and *P*-wave velocity profiles. Fig. 11 shows the inversion results obtained from a three-layer parametrization with a linear increase in the velocity with depth. The first five modes are considered during the inversion. The curve with the lowest rate (Fig. 11a, black) is assumed to be the fundamental mode, the next curve is compared to the first, the second or the third higher mode and the last curve, with the highest rate, can range from the second to the fourth higher modes. To automatically identify higher-order modes, the misfit that is represented by the colour scale is computed with the theoretical

modal curve that provides the best fit. For this parametrization, the experimental dispersion curves are shown to optimally fit the second and the fourth higher-order modes. Note that what was initially considered as interference between the different mode branches in Fig. 10 can also be considered as part of the third higher-order mode.

As expected from the surface wave dispersion curve, the *P*-wave velocity profile is poorly inverted, as no prior information was introduced about its shape and values. Uncertainties in the *P*-wave velocity are included directly in the variability of the *S*-wave velocity profiles. All of the profiles generated are physically consistent with Poisson's ratios within 0.2 and 0.5 (Fig. 11d). Finally, Figs 11(e)–(h) show the *a-posteriori* distribution and the interdependence of some of the inversion parameters: the slope of the velocity gradient versus the *S*-wave velocity for the first and second layers (Figs 11e and g), and the *S*-wave velocity for the second layer versus the depth of the first and second layers (Figs 11f and h).

The parametrization defines high velocity (>1200 m s^{-1}) over the first 50 m, with large uncertainty that covers an increase in velocity from 1200 to 1500 m s^{-1} at depths of around 450 m. Below this interface, strong contrast is expected, and the *S*-wave velocities are not resolved any more. The maximum wavelength of the experimental dispersion curve is 600 m. Resolving the *S*-wave velocity profile down to 450 m (3/4 of a wavelength) is not usual. With
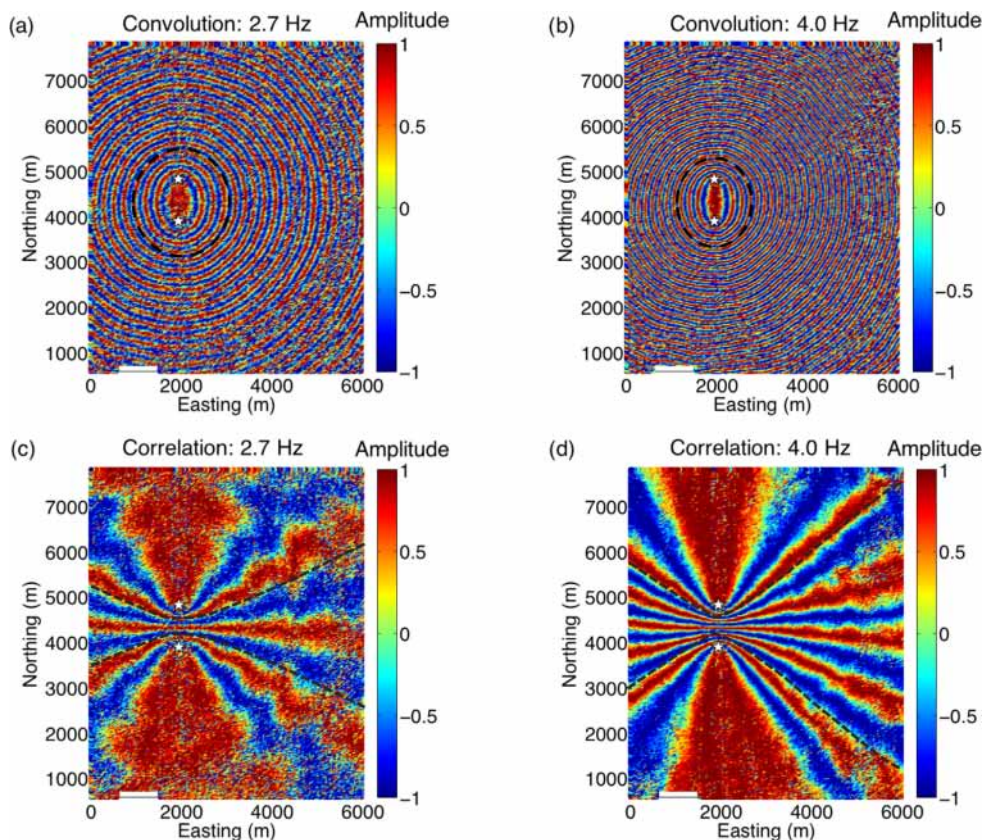
Figure 8. Data-based DKs for convolution (a and b) and correlation (c and d) at the two different frequencies of 2.7 Hz (a and c) and 4.0 Hz (b and d). The distance between the two receivers was 930 m. The *x* and *y* coordinates correspond to source positions $\mathbf{r}_s$. The dashed ellipse and hyperbola correspond to the source position area used for the phase-velocity inversion shown in Fig. 9.
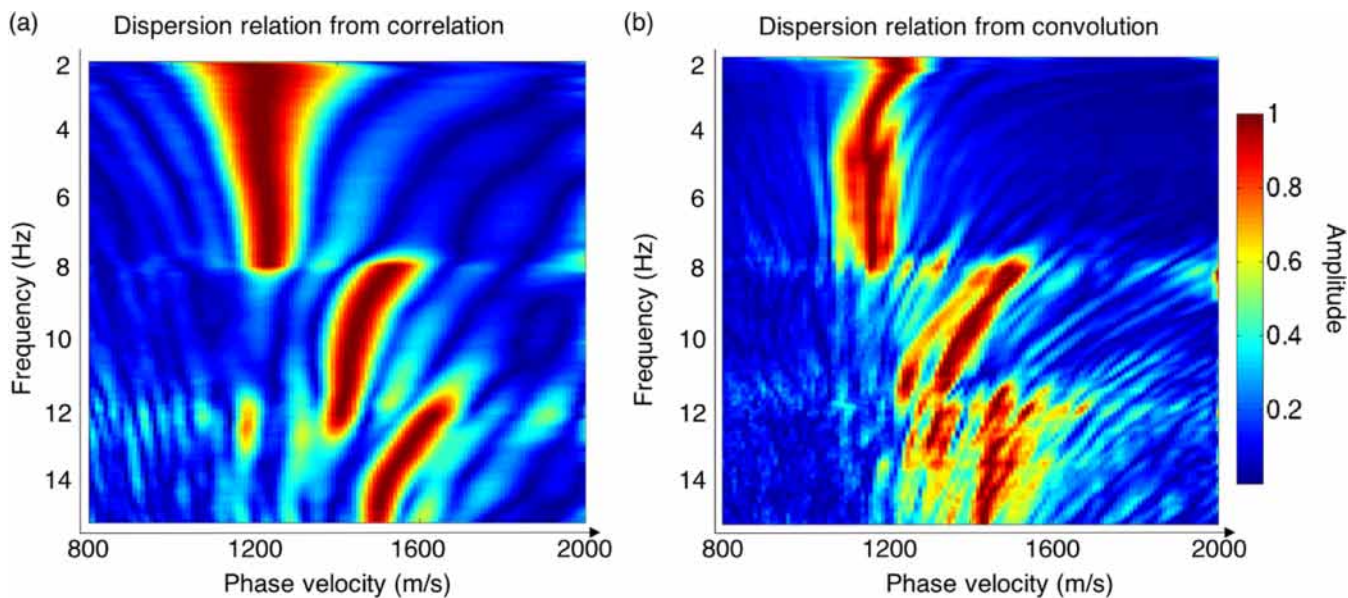
Figure 9. Surface wave dispersion relations obtained from least-squares minimization with L2-norm regularization from a correlation DK (a) and a convolution DK (b).

(a) Least-squares minimization with L1 regularization (b) Least-squares minimization with L2 regularization
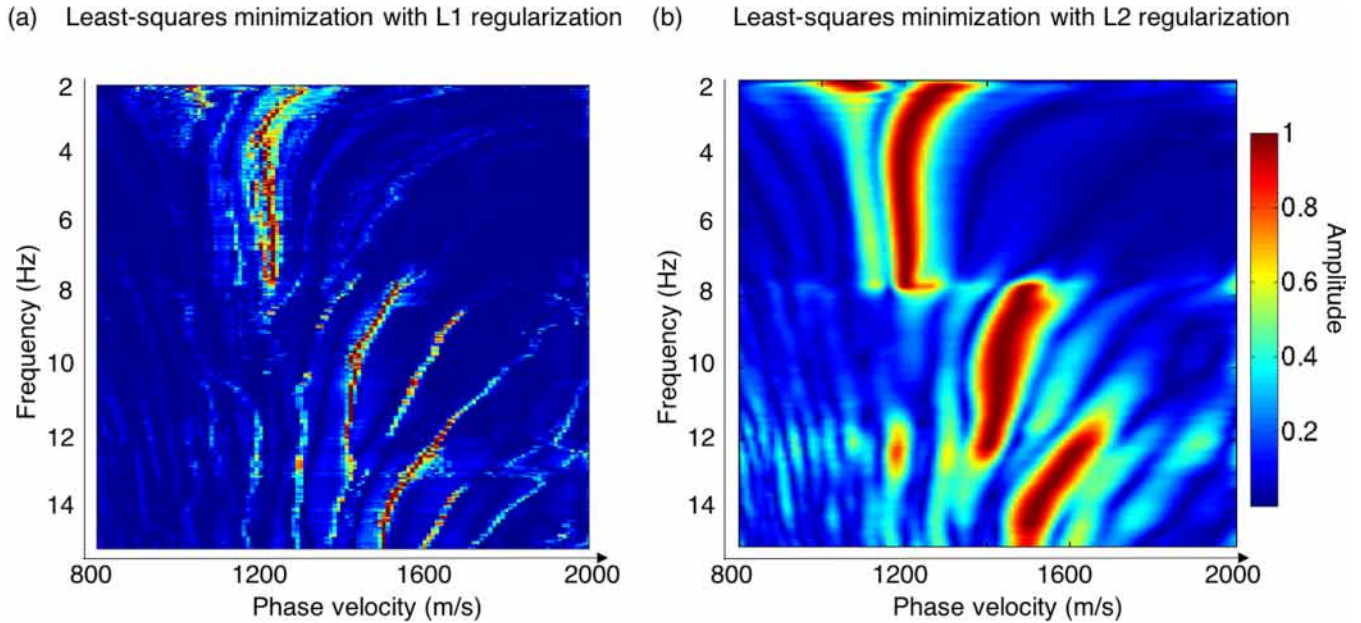
Figure 10. Surface wave dispersion relations obtained from joint inversion based on correlation and convolution DKs. (a) Least-squares minimization with L1-norm regularization. (b) Least-squares minimization with L2-norm regularization.

surface wave inversion performed from the fundamental Rayleigh mode, good resolution can generally be obtained down to a third or a quarter of the maximum wavelength. We checked that the gradient parametrization used for the inversion of the fundamental mode only provides lower resolution and higher uncertainties (Fig. S1, Supplementary Information). In this single-mode inversion, there are much higher uncertainties at all depths of the *S*-wave velocity profile, and a depth resolution limit is seen at around 200 m, which is in agreement with the general relations between penetration depth and maximum available wavelength. This example demonstrates the advantages of multimodal inversion over the classical approach, if the modes are correctly identified. Note that such inversion can be performed for any two points in the medium, which might further result in an accurate tomography map for *V*s. However, this global inversion goes beyond the scope of this paper. Note that there is abundant literature on surface wave inversion from dense arrays of sources and/or receivers using either active or passive data. In the context of geophysics exploration, surface wave inversion provides valuable information about the near-surface that can be used to improve existing models of the subsurface, and for static corrections.

5 DISCUSSION

Benefitting from a detailed data set with a dense sheet of sources and receivers, we present a method to construct data-based surface wave DKs that are simultaneously spatially and frequency dependent and limited to phase representation. These DKs are purely data based, as no wave-propagation model is required, and with the benefit of active sources with absolute time control they are constructed from either correlation or convolution processes. For convolution, these DKs result from a product of recorded wavefields in the frequency domain. They provide information about the spatial extension of the first Fresnel zone in between the two sensors, similar to Lin *et al.* (2010). On the other hand, the correlation DKs

provide spatial information about the stationary-phase area in the alignment of the two sensors, and these can be interpreted as source power spectral DKs, as defined by Walker (2012) and Fichtner *et al.* (2017).

The inversion method allows the retrieval of phase-velocity dispersion relations for any receiver pair in the medium, up to 15 Hz. Dispersion relations from convolutions show better resolution at lower frequencies (due to phase addition in the convolution), while dispersion relations from correlations show more robustness at higher frequencies (due to phase differences in the correlation). This led us to combine both sets of information in a joint inversion process with adequate weighting in the frequency domain. When accumulated over all of the receiver pairs in the medium, each optimal two-point dispersion relation can finally be inverted for local *S*-wave velocity profiles in a global tomography inversion process. This tomography inversion will be shown in our future work.

This data-based DK method can add valuable information about near-surface characteristics, and in particular, allow measurement of statics, which are key issues in geophysics exploration. We can also use the dispersion relations to separate fundamental from higher-order surface wave modes.

We have verified here that the dispersion relations retrieved from the DKs are consistent with dispersion relations calculated using other methods (e.g. spatial Fourier transformation: F-K and frequency-time analysis; Levshin *et al.* 1972). The method we propose presents certain benefits when compared to existing methods. First, the dispersion relations are not aliased due to the irregular distribution of the offsets in the correlation and convolution. Second, they provide dispersion relations between two receiver points by using the whole carpet of sources, which makes the separation of different branches of surface wave higher-order modes much more efficient than the above-mentioned methods. Finally, it would be interesting to study the effects of a reduction in the number of sources on the results obtained for the optimal dispersion relation.
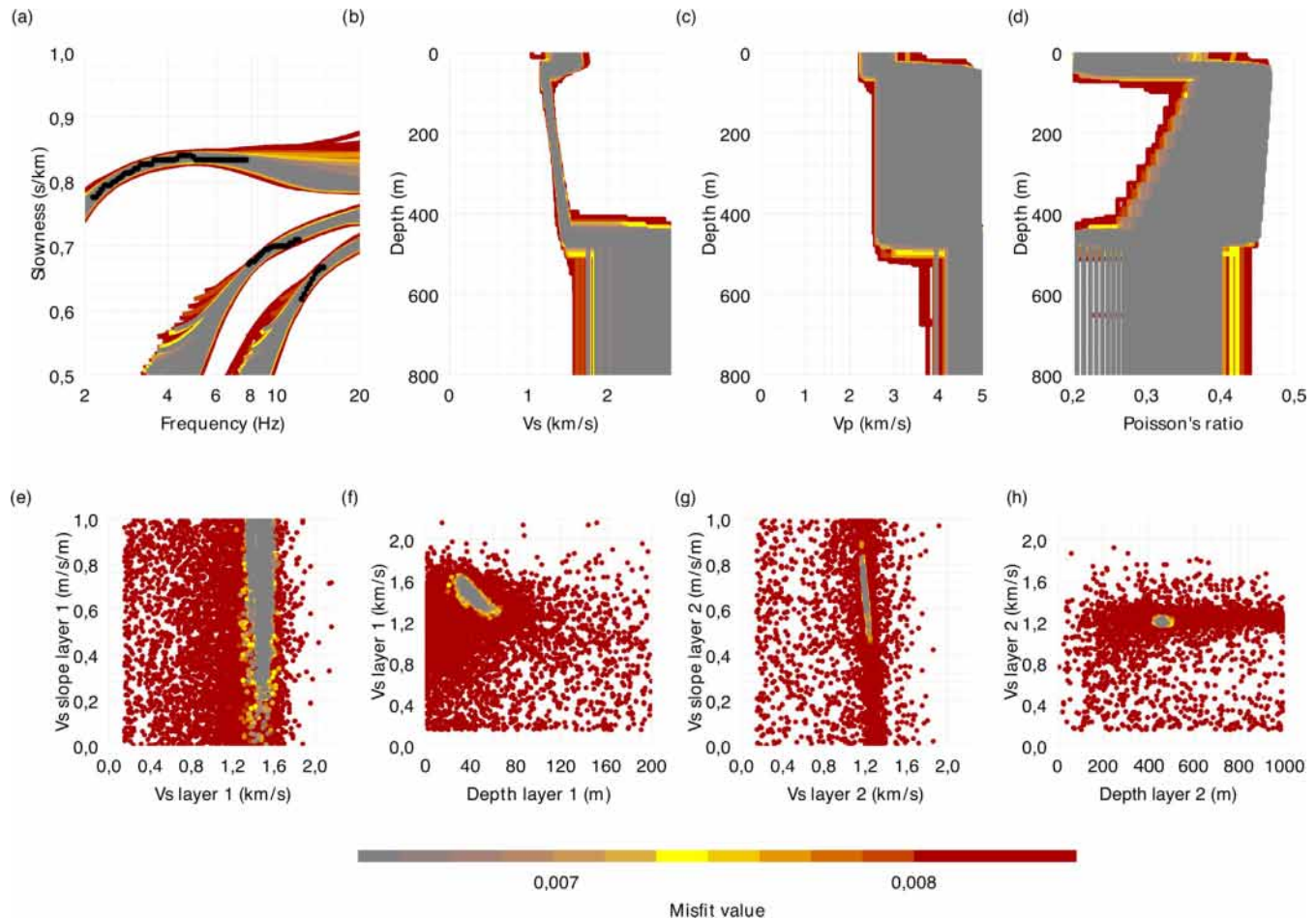
Figure 11. Inversion of the two-point dispersion curve between receivers shown in Fig. 8. (a) Dispersion relations for the fundamental mode and two higher-order overtones (maximum, black). (b) *V*s profile. (c) *V*p profile. (d) Poisson's ratio obtained from the inversion. (e–h) The *a-posteriori* distribution and interdependence of some of the model parameters after inversion. (e) The slope of the gradient versus the *S*-wave velocity for the first layer. (f) The *S*-wave velocity versus the first layer. (g) The slope of the gradient versus the *S*-wave velocity for the second layer. (h) The *S*-wave velocity versus the depth of the second layer.

Other applications can also be envisaged, such as the possibility to extract DKs with correlations and convolutions for other wavefield components. Due to the use of controlled sources, we can focus on exploration of the different components of the recorded wavefield; for example, reflected body waves. Similar investigations can be performed for detection of subsurface reflectors from the coda part of the recorded wavefield following the C3 method that was developed for noise correlation (Stehly *et al.* 2008).

pairs of receivers or pairs of sources. To benefit from the dense acquisition, we extracted frequency-dependent data-based DKs from correlation and convolution two-point measurements of the seismic wavefield. We propose an inversion method based on the phase-only DKs to produce multimodal phase-velocity dispersion relations between two points. Using convolution and correlation with active sources is an important step in understanding the physics of Green's function retrieval. This method provides the foundation for future tomographic studies of high-resolution subsurface structures from surface wave inversion.

6 CONCLUSIONS

Seismic configurations with dense, active, controlled sources recorded on a dense receiver array, as available in land active-seismic data from exploration geophysics, provide more processing possibilities in terms of spatial interferometry. The use of controlled sources makes it possible to recover the surface wave Green's function between two points using either correlation or convolution. Invoking spatial reciprocity between sources and receivers, correlation and convolution functions can be constructed between either

REFERENCES

Bakulin, A. & Calvert, R., 2004. Virtual source: new method for imaging and 4D below complex overburden, in *74th Annual International Meeting, Society of Exploration Geophysicists, Expanded Abstracts,* Denver, CO, pp. 2477–2480.

Barmin, M.P., Ritzwoller, M.H. & Levshin, A.L., 2001. A fast and reliable method for surface-wave tomography, *Pure appl. Geophys.,* **158,** 1351–1375.

Boschi, L. & Weemstra, C., 2015. Stationary-phase integrals in the cross-correlation of ambient noise, *Rev. Geophys.,* **53,** 411–451.

Boyd, S. & Vandenberghe, L., 2004. *Convex Optimization,* Cambridge Univ. Press.

Brenguier, F., Shapiro, N.M., Campillo, M., Nercessian, A. & Ferrazzini, V., 2007. 3-D surface-wave tomography of the Piton de la Fournaise volcano using seismic noise correlation, *Geophys. Res. Lett.,* **34,** L02305, doi:10.1029/2006GL028586.

Campillo, M. & Roux, P., 2014. Seismic imaging and monitoring with ambient noise correlations, in *Treatise on Geophysics,* pp. 256–271, eds Romanowicz, B. & Dziewonski, A., Elsevier.

Chen, S.S., Donoho, D.L. & Saunders, M.A., 1999. Atomic decomposition by basis pursuit, *SIAM J. Sci. Comput.,* **20**(1), 33–61.

Dahlen, F., Hung, S.-H. & Nolet, G., 2000. Frechet kernels for finite-frequency traveltimes – I. Theory, *Geophys. J. Int.,* **141,** 157–174.

de Vos, D., Paulssen, H. & Fichtner, A., 2013. Finite-frequency sensitivity kernels for two-station surface wave measurements, *Geophys. J. Int.,* **194,** 1042–1049.

Duguid, C., Halliday, D. & Curtis, A, 2011. Source-receiver interferometry for seismic wavefield construction and ground-roll removal, *Leading Edge,* **30,** 838–843.

Errico, R. M, 1997. What is an adjoint model? *Bull. Am. Meteorol. Soc.,* **78,** 2577–2591.

Fichtner, A., Bunge, H.-P. & Igel, H., 2006. Theoretical background for the inversion of seismic waveforms, including elasticity and attenuation, *Phys. Earth planet. Inter.,* **157,** 86–104.

Fichtner, A., Stehly, L., Ermert, L. & Boehm, C., 2017. Generalised interferometry - I: theory for interstation correlations, *Geophys. J. Int.,* **208,** 603–638.

Guillouet, M., Berthaud, A., Bianchi, T., Pignot, G., Mahrooqi, S. & Shorter, J., 2016. Recovery of blended data—a sparse coding approach for seismic acquisition normal access, in *78th EAGE Conference and Exhibition 2016, Extended Abstract,* Vienna, Austria, doi:10.3997/2214-4609.201600947.

Halliday, D. & Curtis, A., 2008. Seismic interferometry, surface waves and source distribution , *Geophys. J. Int.,* **175,** 1067–1087.

Hastie, T., Tibshirani, R. & Friedman, J.H., 2001. *The Elements of Statistical Learning,* Springer.

Heaton, T.H., 2005. 'Engineering seismology notes'. Available at: http:// www.its.caltech.edu/~heatont/Eng_Seism_Notes/ch5_surfacewaves.pdf , Access date: November 2017.

Jones, V., 2000. Interaction of radiation and matter'. Available at: https: //archive.org/details/flooved2930, Access date: November 2017.

Levshin, A.L., Pisarenko, V.F. & Pogrebinsky, G.A., 1972. On a frequency-time analysis of oscillations, *Ann. Geophys.,* **128,** 211–218.

Lin, F.-Ch. & Ritzwoller, M. H., 2010. Empirically determined finite frequency sensitivity kernels for surface waves, *Geophys. J. Int.,* **182**(2), 923–932.

Lin, F.-Ch., Ritzwoller, M.H. & Snieder, R., 2009. Eikonal tomography: surface-wave tomography by phase front tracking across a regional broadband seismic array, *Geophys. J. Int.,* **177**(3), 1091–1110.

Liu, Q. & Tromp, J., 2006. Finite-frequency kernels based on adjoint methods, *Bull. seism. Soc. Am.,* **96,** 2383–2397.

Marandet , C., Roux, P., La Rizza, P. & Nicolas, B., 2011. Understanding the feedback effect through the physics of the diffraction-based sensitivity kernel for a target in shallow water: A small-scale experimental demonstration. , *J. acoust. Soc. Am.,* **130,** 2410.

Marquering, H., Dahlen, F.A. & Nolet, G., 1999. Three-dimensional sensitivity kernels for finite-frequency travel-times: the banana–doughnut paradox, *Geophys. J. Int.,* **137**(3), 805–815.

Peter, D., Tape, C., Boschi, L. & Woodhouse, J. H., 2007. Surface wave tomography: global membrane waves and adjoint methods, *Geophys. J. Int.,* **171**(3), 1098–1117.

Postel, J.-J., Meunier, J. & Bianchi, T., 2005. Reduced vibroseis cycle time technique increases land crew productivity, *First Break,* **23**(2), 37–40.

Roux, P, Sabra, K.G., Kuperman, W.A. & Roux, A., 2005. Ambient-noise cross-correlation in free space: theoretical approach, *J. acoust. Soc. Am.,* **117,** 79–84.

Roux, P. & Fink, M., 2003. Green's function estimation using secondary sources in a shallow water environment, *J. acoust. Soc. Am.,* **113**(3), 1406–1416.

Roux, P. & Kuperman, W.A., 2004. Extracting coherent wavefronts from acoustic ambient noise in the ocean, *J. acoust. Soc. Am.,* **116,** 1995–2003.

Sabra, K.G., Gerstoft, P., Roux, P., Kuperman, W.A & Fehler, M., 2005. Extracting time-domain Green's function estimates from ambient seismic noise, *Geophys. Res. Lett.,* **32,** L03310, doi:10.1029/2004GL021862.

Schmidt, M., 2005. Least squares optimization with L1-Norm regularization, Technical report, University of British Columbia, CS542B Project Report.

Schuster, G.T., Yu, J., Sheng, J. & Rickett, J., 2008. Interferometric/daylight seismic imaging, *Geophysics,* **157,** 838–852.

Shapiro, N.M. & Campillo, M., 2004. Emergence of broadband Rayleigh waves from correlations of the ambient seismic noise, *Geophys. Res. Lett.,* **31,** L07614, doi:10.1029/ 2004GL019491.

Shapiro, N.M., Campillo, M., Stehly, L. & Ritzwoller, M.H., 2005. High-resolution surface-wave tomography from ambient seismic noise, *Science,* **307,** 1615–1618.

Sheriff, R.E. & Geldart, L.P., 1995. *Exploration Seismology,* 2nd edn, Cambridge Univ. Press.

Slob, E., Draganov, D. & Wapenaar, K., 2007. Interferometric electromagnetic Green's functions representations using propagation invariants, *Geophys. J. Int.,* **169**(1), 60–80.

Snieder, R., 2004. Extracting the Green's function from the correlation of coda waves: a derivation based on stationary phase, *Phys. Rev. E,* **69,** 046610, doi:10.1103/PhysRevE.69.046610.

Spetzler, J., Trampert, J. & Snieder, R., 2002. The effects of scattering in surface wave tomography, *Geophys. J. Int* **149,** 755–767.

Stehly, L., Campillo, M., Froment, B. & Weaver, R.L., 2008. Reconstructing Green's function by correlation of the coda of the correlation (C^3) of ambient seismic noise, *J. geophys. Res.,* **113,** B11306, doi:10.1029/2008JB005693.

Tarantola, A., 1988. Theoretical background for the inversion of seismic waveforms, including elasticity and attenuation, *Pure appl. Geophys.,* **128,** 365–399.

Tibshirani, R, 1996. Regression shrinkage and selection via the Lasso, *J. R. Stat. Soc. B,* **58,** 267–288.

Tromp, J. & Dahlen, F.A. 1993. Variational principles for surface wave propagation on a laterally heterogeneous Earth – III. Potential representation, *Geophys. J. Int.,* **112,** 195–209.

Tromp, J., Luo, Y., Hanasoge, S. & Peter, D., 2010. Noise cross-correlation sensitivity kernels, *Geophys. J. Int.,* **183,** 791–819.

Tromp, J., Tape, C. & Liu, Q., 2005. Seismic tomography, adjoint methods, time reversal, and banana doughnut kernels, *Geophys. J. Int.,* **160,** 195–216.

van Heijst, H.J. & Woodhouse, J., 1997. Measuring surface-wave overtone phase velocities using a mode branch stripping technique, *Geophys. J. Int.,* **131,** 209–230.

Walker, S.C., 2012. Coherence and interference in diffuse noise: on the information and statistics associated with spatial wave correlations in directional noise fields, *J. acoust. Soc. Am.,* **131**(3), 1987–1998.

Wapenaar, K., 2004. Retrieving the elastodynamic Green's function of an arbitrary inhomogeneous medium by cross-correlation, *Phys. Rev. Lett.,* **93,** 254301, doi:10.1103/PhysRevLett.93.254301.

Wapenaar, K., van der Neut, J. & Ruigrok, E., 2008. Passive seismic interferometry by multidimensional deconvolution, *Geophysics,* **73,** A51–A56.

Wathelet, M., Jongmans, D., Ohrnberger, M. & Bonnefoy-Claudet, S., 2008. Array performances for ambient vibrations on a shallow structure and consequences over Vs inversion, *J. Seismol.,* **12,** 1–19.

Yang, Y. & Forsyth, D.W., 2006. Regional tomographic inversion of the amplitude and phase of Rayleigh waves with 2-D sensitivity kernels, *Geophys. J. Int.,* **166,** 1148–1160.

Yoshizawa, K. & Kennett, B.L.N., 2002. Determination of the influence zone for surface wave paths, *Geophys. J. Int.,* **149**(2), 440–453.

Yoshizawa, K. & Kennett, L. N., 2005. Sensitivity kernels for finite-frequency surface waves, *Geophys. J. Int.,* **162**(3), 910–926.

Zhao, L., Jordan, T.H. & Chapman, C.H., 2000. Three-dimensional Fréchet differential kernels for seismic delay times, *Geophys. J. Int.,* **141,** 558–576.

Zhou, Y., Dahlen, F.A. & Nolet, G., 2004. Three-dimensional sensitivity kernels for surface wave observables, *Geophys. J. Int.,* **158**(1), 142–168.

SUPPORTING INFORMATION

Supplementary data are available at *GJI* online.

Figure S1. Inversion of the two-point dispersion curve between the receivers shown in Fig. 8, with only the fundamental mode of the Rayleigh waves considered in the inversion algorithm.

(a) Dispersion relations for the fundamental mode (maximum, black). (b) *V*s profile. (c) *V*p profile. (d) Poisson's ratio obtained from the inversion. (e–h) The *a-posteriori* distribution and interdependence of some of the model parameters after inversion. (e) The slope of the gradient versus the *S*-wave velocity for the first layer. (f) The *S*-wave velocity versus the first layer. (g) The slope of the gradient versus the *S*-wave velocity for the second layer. (h) The *S*-wave velocity versus the depth of the second layer.

Please note: Oxford University Press is not responsible for the content or functionality of any supporting materials supplied by the authors. Any queries (other than missing material) should be directed to the corresponding author for the paper.